Biomedical Signal Processing and Control 7 (2012) 129–140

Contents lists available at ScienceDirect

Biomedical Signal Processing and Control

journal homepage: www.elsevier.com/locate/bspc

Correction of inhomogeneous magnetic resonance images using multiscale retinex for segmentation accuracy improvement

Wen-Hung Chao[a], Hsin-Yi Lai[b], Yen-Yu I. Shih[c], You-Yin Chen[d,*], Yu-Chun Lo[e], Sheng-Huang Lin[e,f], Siny Tsang[g], Robby Wu[h], Fu-Shan Jaw[e]

[a] Department of Biomedical Engineering, Yuanpei University, No. 306, Yuanpei St., Hsinchu 300, Taiwan, ROC
[b] Department of Electrical Engineering, National Chiao-Tung University, No. 1001, Ta-Hsueh Rd., Hsinchu 300, Taiwan, ROC
[c] Research Imaging Institute, University of Texas Health Science Center at San Antonio, 8403 Floyd Curl Drive, San Antonio, TX 78229-3900, USA
[d] Department of Biomedical Engineering, School of Biomedical Science and Engineering, National Yang-Ming University, No. 155, Sec. 2, Linong St., Taipei 112, Taiwan, ROC
[e] Institute of Biomedical Engineering, College of Medicine, National Taiwan University, No. 1, Sec. 1, Jen-Ai Rd., Taipei 100, Taiwan, ROC
[f] Department of Neurology, Tzu Chi General Hospital, Tzu Chi University, No. 707, Sec. 3, Chung Yang Rd., Hualien 970, Taiwan, ROC
[g] Department of Psychology, University of Virginia, 102 Gilmer Hall, PO Box 400400, Charlottesville, VA 22904-4400, USA
[h] Philadelphia College of Osteopathic Medicine, 4170 City Avenue, Philadelphia, PA 19131, USA

ARTICLE INFO

Article history:
Received 26 August 2010
Received in revised form 5 January 2011
Accepted 5 April 2011
Available online 29 April 2011

Keywords:
Segmentation
Boosted decision tree
Multiscale retinex
Spatial feature
Brain tissue

ABSTRACT

The purpose of this study was to improve the accuracy of tissue segmentation on brain magnetic resonance (MR) images preprocessed by multiscale retinex (MSR), segmented with a combined boosted decision tree (BDT) and MSR algorithm (hereinafter referred to as the MSRBDT algorithm). Simulated brain MR (SBMR) T1-weighted images of different noise levels and RF inhomogeneities were adopted to evaluate the outcome of the proposed method; the MSRBDT algorithm was used to identify the gray matter (GM), white matter (WM), and cerebral-spinal fluid (CSF) in the brain tissues. The accuracy rates of GM, WM, and CSF segmentation, with spatial features (G, x, y, r, θ), were respectively greater than 0.9805, 0.9817, and 0.9871. In addition, images segmented with the MSRBDT algorithm were better than those obtained with the expectation maximization (EM) algorithm; brain tissue segmentation in MR images was significantly more precise. The proposed MSRBDT algorithm could be beneficial in clinical image segmentation.

1. Introduction

The segmentation of brain magnetic resonance (MR) images is a pivotal technique in the assessment of volumetric differences for clinical diagnosis, such as brain tissue and brain tumor segmentation [1–4]. Brain tissue segmentation is an important issue among brain MR image segmentation research [5–8]; there exist several brain tissue segmentation methods for MR image studies. Shen et al. [9] proposed an intelligent segmentation technique to identify brain tissues, including the gray matter (GM), white matter (WM), and cerebral spinal fluid (CSF), in brain MR images. A neighborhood attraction, which includes pixel intensities (feature attraction), spatial position of neighbors (distance attraction), and improved fuzzy c-means (FCM), was used to improve segmentation accuracy. In addition, the degree of feature attraction and distance attraction was optimized by an artificial neural-network model. This technique was an improvement from the traditional FCM algorithm; simulated T1-weighted MR images with different noise levels and real MR images were segmented for better results. Vrooman et al. [10] presented a new, fully automatic k-Nearest-Neighbor (KNN) training procedure with non-rigid registration to identify brain tissues; results showed improved accuracy in the segmentation of GM, WM, and CSF. This robust segmentation performance was also evaluated with a similar index (SI). Manjon et al. [11] proposed a tissue type parameter estimation method to estimate mean intensity values of GM, WM, and CSF accurately. As indicated from the preponderous amount of literature, improving the accuracy of brain tissue segmentation in MR images is important for the identification of GM, WM, and CSF for neuro-imaging application.

The signal to noise ratio (SNR) of MR images is sometimes reduced by the receive coils. The image quality is affected by the decreased SNR. In general, the surface coil provides better SNR than the volume coil during MR image acquisition. The surface coil often generates radio-frequency (RF) inhomogeneities when acquiring MR signals. However, RF inhomogeneity, as well as the background noise and partial volume effect, reduces the accuracy of tissue segmentation for brain MR images. Attempts have been

* Corresponding author. Tel.: +886 2 2826 7000x7022; fax: +886 2 2608 0963.
E-mail address: irradiance@so-net.net.tw (Y.-Y. Chen).

1746-8094/$ – see front matter © 2011 Elsevier Ltd. All rights reserved.
doi:10.1016/j.bspc.2011.04.001

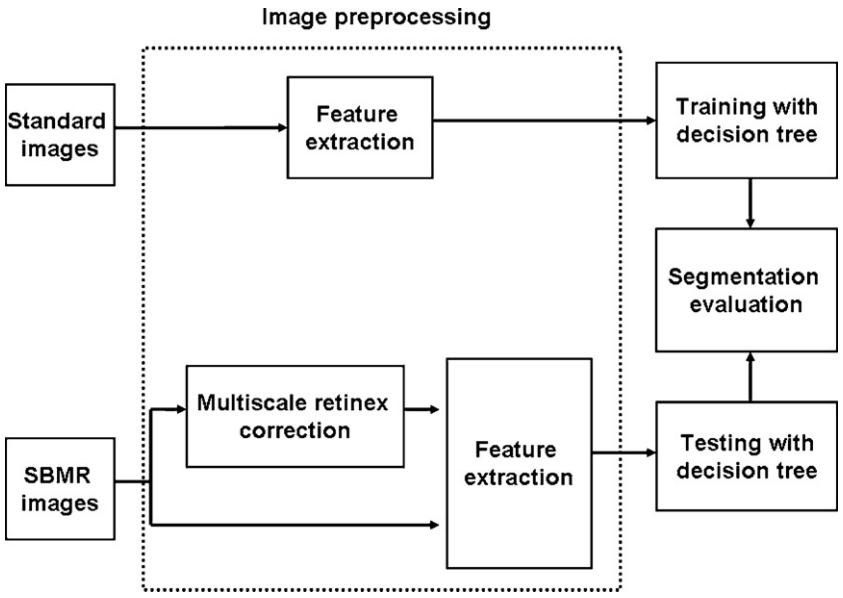

Fig. 1. Image processing procedures.

made to minimize segmentation errors of MR images with correction algorithms. A robust automatic algorithm with correcting radio-frequency (RF) inhomogeneity has been designed to segment GM, WM, and CSF of MR images in phantom studies and clinical experiments [12]. Gispert et al. [13] proposed a nonuniform intensity correction (NIC) algorithm (bias field estimation and tissue classification) to segment the phantom dataset and the real image dataset. The NIC algorithm showed the best performance for classifying GM, WM, and CSF in T1-weighted MR images on phantom and real images. Garcia-Sebastian et al. [14] proposed a parametric intensity inhomogeneity (IIH) correction schema and an online estimation of the image model intensity class means to segment MR images. Several previous studies [12–15] have demonstrated brain tissue segmentation with decreased noise-induced errors. However, segmentation errors were increased due to RF inhomogeneities. In an effort to resolve this problem, we proposed a boosted decision tree (BDT) combined with the multiscale retinex (MSR) algorithm (hereinafter referred to as the MSRBDT algorithm) as a preprocessing process. The retinex algorithm was used to reduce the nonuniformity of MR images caused by RF inhomogeneity in MR image intensity. Land [16] proposed a retinex model based on the neurophysiological processing of brain image information in retinas to describe color constancy in human visual perception. The model was developed according to the concept that human perception is not defined solely by the spectral character of the light that reaches the eye; it includes the processing of spatial-dependant color and intensity information on the retina. The process is accomplished by computing dynamic-range compression and color rendition [16–20]. Accordingly, Hurlbert and Poggio [17] and Hurlbert [18] derived a general mathematical function by applying the retinex properties and luminosity principles. Images from various center/surrounding functions in three gray-level scales show different retinex outputs. Moreover, Jobson et al. [21] found that the selection of surrounding function parameters has a significant effect for the retinex output [21,22]. The dynamic compression and color rendition were then balanced with MSR. Although the inhomogeneities of MR image could be reduced with improved hardware, it would be more feasible to develop a preprocessing algorithm to improve the segmentation of brain MR images. The current MSR was hereby proposed for the preprocessing of brain MR images.

After preprocessing, the brain tissues of MR images were segmented with decision tree algorithms. Two decision trees have been developed in existing literature: the classification and regression tree (CART) and the See5/C5.0 (BDT). The CART is a binary tree that can be used for classification and regression analysis [23–26]; the See5/C5.0 [27–29] was advanced from the ID3 learning tree [30] and has been adopted for various biomedical applications [31]. In the previous study, a BDT was applied as the segmentation algorithm as it can effectively classify data structure, predict the accuracy of non-linear problems, interpret rules in a decision tree rule set, and eliminate outliers [25]. Combining the advantages of the MSR and the BDT decision trees, the MSRBDT algorithm was proposed for the identification of GM, WM, and CSF in brain tissues. The goal of the current study was to improve the accuracy rates of brain MR image segmentation.

2. Materials and methods

Image processing procedures are shown in Fig. 1. The decision tree structure was constructed by a training procedure from a standard image (manually identified by an expert), which was tested to identify different types of brain tissues for all brain MR images. Two image preprocessing methods are available for the testing procedure. The first method applies the MSR algorithm to correct for RF inhomogeneities of MR images; spatial features were extracted from the corrected MR images, the images were then segmented. An alternative method is to segment the brain MR images after extracting spatial features. Two decision trees, CART and BDT, were used to evaluate the results of segmented brain images.

2.1. MR images

The simulated brain MR (SBMR) images obtained from BrainWeb (http://www.bic.mni.mcgill.ca/brainweb) were T1-weighted 3-mm-thick images with 3%, 5%, 7%, and 9% noise levels. At each noise levels, RF inhomogeneities of 20% or 40% were introduced to the SBMR images. Details of the SBMR images are described in Table 1. Segmentation results from images of different qualities were examined. An expert manually identified a standard brain MR image from an original image with no noise and inhomogeneity as a training data; it was adopted as the standard image in the present

Table 1
Designations of original simulated MR images obtained by combining the noise levels and inhomogeneities.

Designation	Noise level and inhomogeneity parameters
T1n3	Noise level = 3%
T1n5	Noise level = 5%
T1n7	Noise level = 7%
T1n9	Noise level = 9%
T1n3RF20	Noise level = 3% and 20% RF inhomogeneity
T1n5RF20	Noise level = 5% and 20% RF inhomogeneity
T1n7RF20	Noise level = 7% and 20% RF inhomogeneity
T1n9RF20	Noise level = 9% and 20% RF inhomogeneity
T1n3RF40	Noise level = 3% and 40% RF inhomogeneity
T1n5RF40	Noise level = 5% and 40% RF inhomogeneity
T1n7RF40	Noise level = 7% and 40% RF inhomogeneity
T1n9RF40	Noise level = 9% and 40% RF inhomogeneity

study. The SBMR images were preprocessed with correction or feature extraction at different noise levels and RF inhomogeneities, which were then segmented with decision tree algorithms.

2.2. Image preprocessing

Image preprocessing procedures are shown in Fig. 1 and described as follows. In the training course, spatial features were extracted from the standard image for image preprocessing. In the testing course, two image preprocessing methods were utilized. The first method applied the MSR algorithm to correct for RF inhomogeneities of MR images, after which the spatial features were extracted. For the second method, the spatial features were only extracted for image preprocessing.

2.2.1. Multiscale retinex for RF inhomogeneity correction

Image quality and segmentation accuracy are affected by RF inhomogeneities in MR images; the MSR was thus used to resolve this problem. An MSR [16] consistent with the processing mechanisms of human vision, in terms of dynamic-range compression and brightness variations of the image, was proposed as a preprocessing step to correct RF inhomogeneities in MR images. The MSR was constructed by merging three single-scale retinex (SSR) scales with three weightings [21,22]; the SSR algorithm was utilized to support different dynamic-range compressions [21,22]. The MSR can replicate human visual processing by manipulating an acquired image to correspond to the real grayscale variations of a scene. Research has indicated that dynamic-range compression was more significant than brightness variations in acquired images [21,22]; thus, the present study emphasized on the dynamic-range compression computation of such images. Since results obtained from the MSR were similar to observations of a real scene [16–22], a retinex algorithm was applied to improve the contrast histogram and image quality prior to image preprocessing.

The basics of an SSR [16] were described as follows. Based on a center/surround organization, a logarithmic photoreceptor function that approximates the vision system was applied [16,22]. The SSR was indicated by

$$R_i(x,y) = \log\ I_i(x,y) - \log[(I_i(x,y) * F(x,y)], \tag{1}$$

where $R_i(x,y)$ was the retinex output, $I_i(x,y)$ was the image distribution in the i-th spectral band, and "*" represented the convolution operator. In addition, $F(x,y)$ was defined in Eq. (8) and

$$\iint F(x,y)\ dx\,dy = 1, \tag{2}$$

which was the normalized surround function. The purpose of the logarithmic manipulation was to transform a ratio at the pixel level to a mean value for a larger region.

SSR was applied to each spectral band to improve the luminosity, as suggested by Land [16]. It was independent from the spectral distribution of a single-source illumination since

$$I_i(x,y) = S_i(x,y)r_i(x,y), \tag{3}$$

where $S_i(x,y)$ was the spatial distribution on an illumination source, $\bar{S}_i(x,y)$ represented the spatially weighted average value, and $r_i(x,y)$ was the reflectance distribution in an image, hence

$$R_i(x,y) = \log \frac{S_i(x,y)r_i(x,y)}{\bar{S}_i(x,y)\bar{r}_i(x,y)}. \tag{4}$$

However, there is a great overlap of the Fourier spectra between $S_i(x,y)$ and $\bar{S}_i(x,y)$. There is no use of MRI inhomogeneity correction and then the illumination inhomogeneity is assumed as

$$S_i(x,y) \approx \bar{S}_i(x,y), \tag{5}$$

so this approximate equation was the reflectance ratio

$$R_i(x,y) \approx \log \frac{r_i(x,y)}{\bar{r}_i(x,y)}, \tag{6}$$

which was equivalent to illumination variations.

Hurlbert and Poggio [17] and Hurlbert [18] used the Gaussian surround function to reconcile natural and human vision. With a space constant, the inverse-square surround function accounted for a greater response from the neighboring pixels than the exponential and Gaussian functions. The spatial response of the exponential surround function was larger than that of the Gaussian function at distant pixels. The Gaussian surround function was generally used in regional dynamic-range compression [21], they were able to produce good dynamic-range compression over neighboring pixels [17,20,21]. Among the proposed surround functions in [19–22], the Gaussian surround function demonstrated good performance over a wider range of space constants. Heretofore, the present study adopted the Gaussian surround function to enhance contrasts and resolve the inhomogeneity of MR images.

The final process output from the center/surround retinex could be adjusted to produce the SSR output [16]. Moore et al. [19] proposed an automatic gain and offset operation, in which the triplet retinex outputs were regulated by the absolute maximum and minimum values of all scales in a scene. In this study, a constant gain and offset technique was used to select the best rendition, as well as the transferred output interval of the highest- and lowest-scale rendition scenes for each SSR. There was no significant information loss due to adjustments to the gain and offset result in the retinex outputs; the constant gain and offset of the retinex was independent of the image content. Histogram variations in a gray-level scene were evaluated. The gain and offset were constant across images according to Land's algorithm [16], an indication that it is applicable for the manipulation of most images.

The best value of scale factor c was selected for the surround function, $F(x,y)$, based on the dynamic range compression and brightness rendition for each SSR. The dynamic range compression and brightness rendition were also optimized by the selected scale factor c and the adjustment of SSR output. The MSR was a good method for summing a weighted SSR to mix the SSR output variations, which was defined as

$$R_{\mathrm{MSR}_i} = \sum_{i=1}^{N} \omega_i R_{ni}, \tag{7}$$

where N was a scaling parameter, R_{ni} was the i-th component of the n-th scale, R_{MSR_i} was the n-th spectral component of the MSR output, ω_i was the multiplication weight for the i-th scale, and the

sum of ω_i was equal to 1 ($i = 1, \ldots, N$). $R_i(x, y)$ of Eq. (6) became R_{ni} in Eq. (7) where

$$F_n(x, y) = Ke^{-r^2/c_n^2} \tag{8}$$

and

$$r = \sqrt{x^2 + y^2}. \tag{9}$$

Combining various SSR weightings [21,22], the MSR selected the number of scales used for the application and evaluated the number of scales that could be merged. The numbers of scales and scaling values in the surround function, as well as the weights in the MSR were issues of concern. MSR was implemented by a series of MR images, based on a trade-off between dynamic-range compression and brightness rendition. Also, weights were accordingly selected to obtain the appropriate dynamic-range compression at the light and dark boundaries of the image, as well as to maximize the brightness rendition of the entire image. MSR results on visual rendition were verified with a series of MR images. Furthermore, the efficacy of the MSR technique in MR image contrast enhancement was compared with other image processing techniques.

Previous literature has proposed an algorithm for MSR applicable in human vision [21,22]. By comparing the psychophysical mechanisms between human visual perceptions of a real scene and a captured image, as well as comparing the captured image with the measured reflectance values of the real scene, MSR compensated for lighting variations to approximate human perceptions of a real scene. The present method combined specific features of MSR with the SSR process, in which a Gaussian function was adopted for the center/surround operation. A narrow Gaussian distribution was used for the neighboring areas of a pixel (regarded as the center). Space constants for Gaussian functions with scales of 15, 80, and 250 pixels in the surrounding area, as proposed by Jobson et al. [21,22], were adopted. Logarithm was then applied after surround function processing (i.e., two-dimensional spatial convolution). Next, appropriate gain and offset values were determined according to the retinex output and the histogram characteristics; these values remained constant for all images. The MSR function was hence obtained.

2.2.2. Feature extraction

Spatial features were extracted from every MR image pixel location; they were used as the segmentation algorithm input for image preprocessing. The spatial features used in the present study were: G, S, x, y, r, and θ, where G was the gray level intensity of every pixel, S was the spatial gray level of every pixel, (x, y) were the Euclidean coordinates, and (r, θ) were the polar coordinates. The spatial features of the general gray level, and spatial gray level were combined in Euclidean (x, y) or polar coordinates (r, θ) through image preprocessing. As the quality of MR images was often affected by noise and RF inhomogeneities, their effect on segmentation accuracy needs to be reduced by image manipulation.

The general gray level represented the intensity of each pixel for MR image segmentation. It was suggested that the accuracy of image segmentation was improved by the enhanced image spatial features used. The spatial gray (S) level is shown in Fig. 2 and defined as

$$S(x, y) = \sum_{i=1}^{n} \omega_i g_i(x, y), \tag{10}$$

which is the sum of combined weighting ω_i and gray level $g_i(x, y)$ of pixel i on the neighboring area. The neighboring area weighting of the gray level around the center pixel with the nearest four pixels are $n = 5$ and $\omega_i = 1/5$.

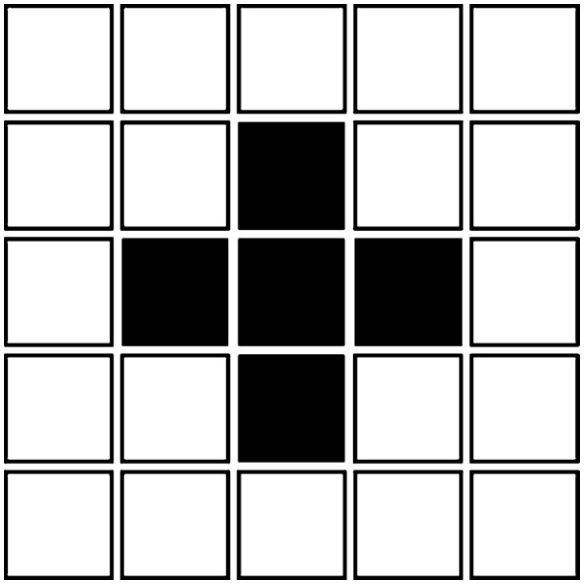

Fig. 2. The spatial gray (S) level is defined as the center pixel and with the nearest four pixels.

2.3. Segmentation

A decision tree combined with boost trials of segmentation method was used in this study. Quinlan [29] proposed to model the prediction tree with statistical analysis, taking into account the outcome variables and decision question for an accurate prediction. The procedure was described as follows.

2.3.1. Decision tree classification

A classifier structure form that could be integrated with boosting and fuzzy threshold was constructed with the decision tree [27–29]. The brain tissues (GM, WM, and CSF) of the SBMR images were segmented with the decision tree algorithm. As shown in Fig. 3, a decision tree is a tree structure growing from a root node of the tree, which flows toward the internal nodes and terminates at the leaf nodes. The leaf nodes represent the class; a classifier is a model built from the training dataset, applied to predict the

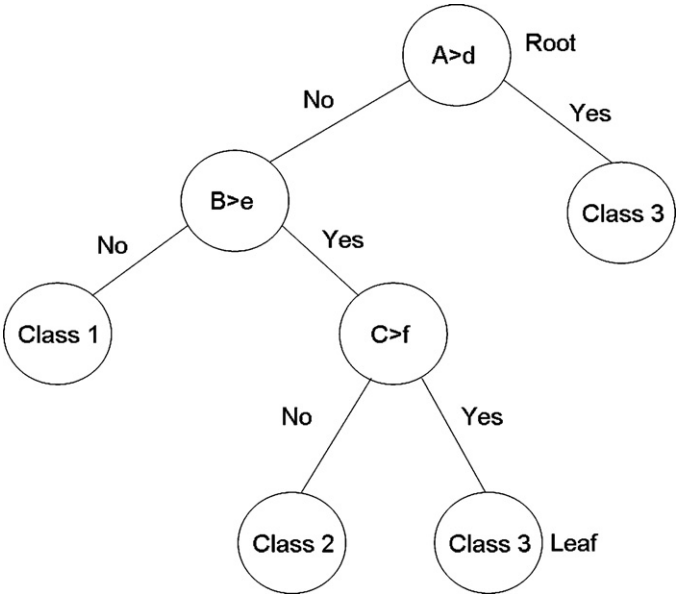

Fig. 3. A schematic example of a decision tree structure.

class values in a test dataset. Each internal node of the tree structure is divided by a condition related to a feature, and each branch denotes the outcome of attribute splitting. Each node (root node and internal node) is split into two or more branch nodes. Examples of the splitting condition are "A > d", "B > e", or "C > f", for each node in every attribute. Branch splitting is determined by the node's condition. The leaf nodes indicate that the classes are classified by the splitting conditions, with the corresponding class labeled on each leaf node. A decision tree structure is then constructed. In addition, the fuzzy threshold can reduce the effects of noise to build classification structure. Each feature partition and node is also determined by the fuzzy threshold process [27,29]. The branches of the feature values are constructed according to probability within the fuzzy threshold to determine the partition for approaching the classification sensitivity.

2.3.2. Decision tree construction with Gain Ratio

The proposed decision tree was constructed from a data set S with the training criteria; *Gain Ratio* was a measure of incorporated entropy [27–30]. The procedures of *Gain Ratio* criteria were described as follows. For simulated MR data, assume that a training data set S consists of C class examples. The function $p(S, r)$ is the ratio of the MR data set class number from class r, with a total class number $|S|$ in a MR data set S, where $1 \le r \le C$. The entropy is defined as

$$Entropy(S) = -\sum_{r=1}^{C} p(S, r) \times \log_2\ p(S, r). \tag{11}$$

Suppose T is a feature with v total partitions. The value i is any v, and S_i is a subset of MR data set S corresponding to the value i of T. The information gain, $Gain(S, T)$, corresponding to the partitioning of S from the feature T, is calculated with

$$Gain(S, T) = Entropy(S) - \sum_{i=1}^{v} \frac{|S_i|}{|S|} \times Entropy(S_i), \tag{12}$$

where $|S|$ is the number of subset S_i in the MR data. $Entropy(S_i)$ is similarly defined as $Entropy(S)$. Bias was reduced to obtain good generation; the gain ratio $Gain\ Ratio(S, T)$ was calculated where the *Split info* (Eq. (14)) is first defined as

$$Split\ Info(S, T) = -\sum_{i=1}^{v} \frac{|S_i|}{|S|} \times \log_2 \left(\frac{|S_i|}{|S|} \right). \tag{13}$$

Because the function $Gain(S, T)$ was very sensitive to the value of v, the ratio of information gain was manipulated as

$$Gain\ Ratio(S, T) = \frac{Gain(S, T)}{Split\ Info(S, T)}. \tag{14}$$

The feature T satisfying

$$\Gamma = arg\max_{T}(Gain\ Ratio(S, T)) \tag{15}$$

was selected as the reference in this step of partitioning. The decision tree was constructed by splitting all of the features and maximizing the gain ratio (Γ).

2.3.3. Boosting

Boosting may also be included in the decision tree to improve the predicted segmentation accuracy rate. It is known as adaptive boosting [27,29,32]. Adaptive boosting is conducted based on the learning algorithm of the decision tree classifier over the repeated series of trials, $t = 1, \ldots, T$. One possible approach is to select the best weight and tree structure from the distribution of weights over the training set. In boosting, multiple classifiers are constructed from a single training dataset. A classifier is constructed to form a decision tree structure or a rule set with the training data. When a new case is classified by a classifier, the predicted class and the final class are decided based on votes from multiple classifiers. The first step of boosting is to build a decision tree structure or a rule set from the training data. In some cases, boosting results in errors in which the wrong class is generated by the first decision tree structure. Next, the second classifier is constructed, focusing on obtaining the correct cases. Thus, the tree structure of the second classifier differs from the first. Accuracy of the cases is further emphasized for the third classifier, even though the possibility of errors remains. By setting the number of boost trials in advance, the boosting process continues with each iteration. The boosting process is terminated when the most recent classifier is either highly accurate or inaccurate.

2.3.4. Pruning

The construction of a decision tree is a two-phase process [27,30]. The decision tree is initially generated in the growth phase, followed by the pruning phase. The pruning phase is used to optimize the structure of the decision tree; global pruning was selected in the present algorithm. Subtree replacement was conducted in the pruning step to reduce the subtree error rates for the training set. If error generation was improved, the nodes of tree structure were trimmed, replacing the subtree with a leaf node. The class label of the leaf node was then defined as a simplified tree with a class of attributes in a subtree. The purpose of pruning was to reduce the risk of tree overfitting; overfitting occurs when the learned tree is overspecialized to the training set. The pruning phase was developed to improve the accuracy rates of classification and to build the tree structures.

2.4. Evaluation of segmentation performance

Accuracy rate was used to quantify the performance of segmentation in this present study. It was compared by overlapping the standard reference image (manually labeled by an expert) with a segmented image obtained from the proposed segmentation method. The accuracy rate (AR) was calculated as the overlap fraction of the two images [9,10,33], defined as

$$\text{Accuracy rate} = \frac{Ref(k) \cap Seg(k)}{Ref(k)}, \tag{16}$$

where the accuracy rate of the segmented area in class k is relative to the area in the standard image. Three classes (GM, WM, and CSF) of SBMR images were segmented in this study. The numerator in Eq. (16) represented the number classified or the intersection area of class k voxels between the segmented image and the standard image. The denominator represented the area of class k voxels in the standard image.

The similarity index (SI), as defined in Eq. (17), was the Dice coefficient; it was frequently used to measure the similarity of two images in previous studies [9,10,33]. It was also used as an alternative evaluation index to quantify the performance of segmentation. SI was defined as

$$\text{Similarity index} = \frac{2|S_1 \cap S_2|}{|S_1| + |S_2|}. \tag{17}$$

Given two binary images, S_1 represented the standard image (manually labeled by an expert), while S_2 represented the segmented image. The $|S_1 \cap S_2|$ represented the number of binary image that were assigned to the tissue between S_1 and S_2. It could also be rewritten as

$$\text{Similarity index} = \frac{|S_1 \cap S_2|}{(1/2)(|S_1| + |S_2|)}. \tag{18}$$

The similarity index, ranging from 0 to 1, was applied to compare the segmented image and standard image.

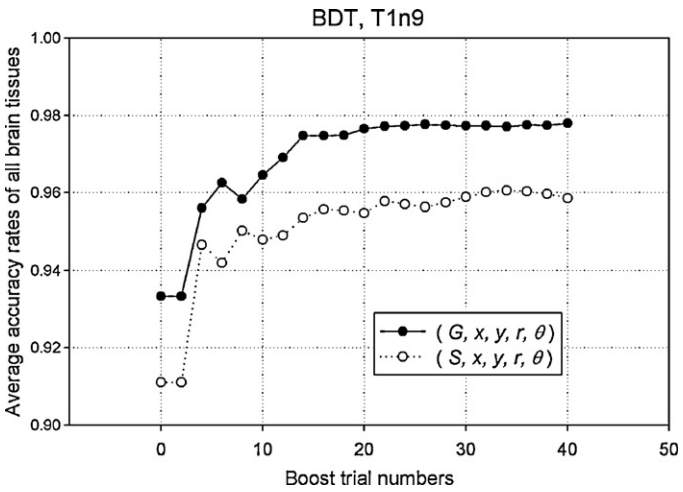

Fig. 4. Average accuracy rates of all brain tissues segmented using the BDT with spatial feature (G,x,y,r,θ) and (S,x,y,r,θ) for different boost trial numbers.

3. Results

3.1. Results of images

In order to obtain the appropriate number of boost trials, the SBMR images with T1n9 were tested with the boosted decision tree, from trial 0 to 40. The MSR was not used in this test for image preprocessing to ascertain that the BDT segmentation was not affected. Average segmentation accuracy rates of BDT with spatial feature (G,x,y,r,θ) and (S,x,y,r,θ) from SBMR images with T1n9 are shown in Fig. 4. The amount of time consumed increased as more boost trials were applied, yet the accuracy rates (ARs) of segmentation decreased with less boost trials. As the optimal ARs of brain tissue segmentation (GM, WM, and CSF) were obtained using the decision tree at 20 boost trials, the decision tree with 20 boost trials was adopted to form the BDT for segmentation on all SBMR images (see Fig. 4).

Images in rows 1 and 2 of Fig. 5 were the T1n3RF20 and T1n9RF40 of SBMR images, respectively. The original images and images corrected with MSR algorithm are respectively presented in columns 1 and 2 of Fig. 5. The corrected images showed more brightness and contrast of brain tissue than the original images. In the present study, the weight ω_n and the MSR scale were combined with the 15-pixel small-scale SSR weightings of $\omega_1 = 1/3$, 80-pixel moderate-scale SSR weightings of $\omega_2 = 1/3$, and 250-pixel large-scale SSR weightings of $\omega_3 = 1/3$ [21,22]. Images segmented by the MSRBDT algorithms with spatial feature (G,x,y,r,θ) are presented in column 3 of Fig. 5. The brain tissues (GM, WM, and CSF) were clearly identified with the MSRBDT algorithm.

3.2. Segmentation of SBMR images

Segmentation results using CART and BDT from SBMR images with T1n3RF20, T1n5RF20, T1n7RF20, and T1n9RF20 are shown in Figs. 6 and 7. Spatial features (G,x,y,r,θ) and (S,x,y,r,θ) for feature extraction with combined-MSR and non-MSR were used for image preprocessing. The AR curve plots of GM, WM, and CSF from SBMR images are shown in rows 1, 2, and 3 of Figs. 6 and 7. The AR curve plots of brain tissue segmentation using CART with spatial features (G,x,y,r,θ) and (S,x,y,r,θ) are respectively presented in Fig. 6. Brain tissue segmentation results using BDT with spatial features (G,x,y,r,θ) and (S,x,y,r,θ) are respectively shown in the curve plots in Fig. 7. The BDT algorithm attained higher segmentation ARs than the CART algorithm. The ARs showed significant improvement when the MSRBDT algorithm and the MSR algorithm with spatial features (G,x,y,r,θ) and (S,x,y,r,θ) were applied. The optimum ARs were achieved when the MSRBDT algorithm with spatial feature (G,x,y,r,θ).

Segmentation results using CART and BDT from SBMR images with T1n3RF40, T1n5RF40, T1n7RF40, and T1n9RF40 are shown in Figs. 8 and 9, respectively. Spatial features (G,x,y,r,θ) and (S,x,y,r,θ) for feature extraction with combined MSR and non-MSR were used for image preprocessing. The AR curve plots of GM, WM, and CSF from SBMR images are shown in rows 1, 2, and 3 of Figs. 8 and 9. Brain tissue segmentation results using CART with spatial features (G,x,y,r,θ) and (S,x,y,r,θ) are respectively presented in the curve plots in Fig. 8. Brain tissue segmentation results segmented by using BDT with spatial features (G,x,y,r,θ) and (S,x,y,r,θ) are respectively shown in the curve plots in Fig. 9. The BDT algorithm attained higher segmentation ARs than the CART algorithm. ARs showed significant improvement when the MSRBDT algorithm with spatial features (G,x,y,r,θ) and (S,x,y,r,θ) were utilized. The highest ARs were achieved when the MSRBDT algorithm with spatial feature (G,x,y,r,θ) was applied.

Segmentation results from the MSRBDT algorithm, as evaluated by accuracy rate and similar index, were also compared with those obtained from expectation maximization (EM) algorithm through adaptive segmentation [34]. For T1n3RF20, T1n5RF20, T1n7RF20, and T1n9Rf20 SBMR images, ARs and similar indices (SIs) of segmentation using the BDT combined with non-MSR, the BDT combined with MSR, and the EM algorithm with spatial feature (G,x,y,r,θ) are presented in Table 2. The SIs of segmented GM were respectively greater than 0.9572, 0.9805, and 0.7252. The SIs of segmented WM were respectively greater than 0.9594, 0.9817, and 0.7570. The SIs of segmented CSF were respectively greater than 0.9759, 0.9871, and 0.5995. For T1n3RF40, T1n5RF40, T1n7RF40, and T1n9Rf40 SBMR images, ARs and SIs of segmentation using the BDT combined with non-MSR, the BDT combined with MSR, and the EM algorithm with spatial feature (G,x,y,r,θ) are shown in Table 3. The SIs of segmented GM were respectively greater than 0.9528, 0.9809, and 0.7270. The SIs of segmented WM were respectively greater than 0.9554, 0.9819, and 0.7699. The SIs of segmented CSF were respectively greater than 0.9769, 0.9857, and 0.5927.

4. Discussion

For T1n9 SBMR images, the BDT algorithm with spatial feature (G,x,y,r,θ) attained higher segmentation accuracy than that with spatial feature (S,x,y,r,θ) (see Fig. 4). Twenty boost trials were adopted to construct the BDT segmentation algorithm with spatial features (G,x,y,r,θ) and (S,x,y,r,θ) for a series test (boost trial 0–40) from a T1n9 SBMR image (Fig. 3). As the number of boost trials increased, the amount of time required for computation increased. High image intensity distribution overlap is often caused by increased noise levels or RF inhomogeneities in SBMR images, affecting segmentation accuracy. The BDT decision tree combined with MSR algorithm was hereby proposed as a solution. The contrasts of brain tissues were enhanced and RF inhomogeneities were corrected with the MSR algorithm (see Fig. 5). Boyes et al. [37] used N3 algorithm to correct brain MR images; an estimated Gaussian distribution of image intensities was used to obtain an estimate of the non-uniformity field. The MSR [22] algorithm uses a Gaussian surround space to estimate the bias field of images. The MSR algorithm is easy to be implemented when combined with three SSRs. These two correction algorithms used a similar function to fit the intensity distribution. The brain tissues of images segmented by BDT with spatial feature (G,x,y,r,θ) from the MSR-corrected images showed enhanced clarity as compared to the original images(see

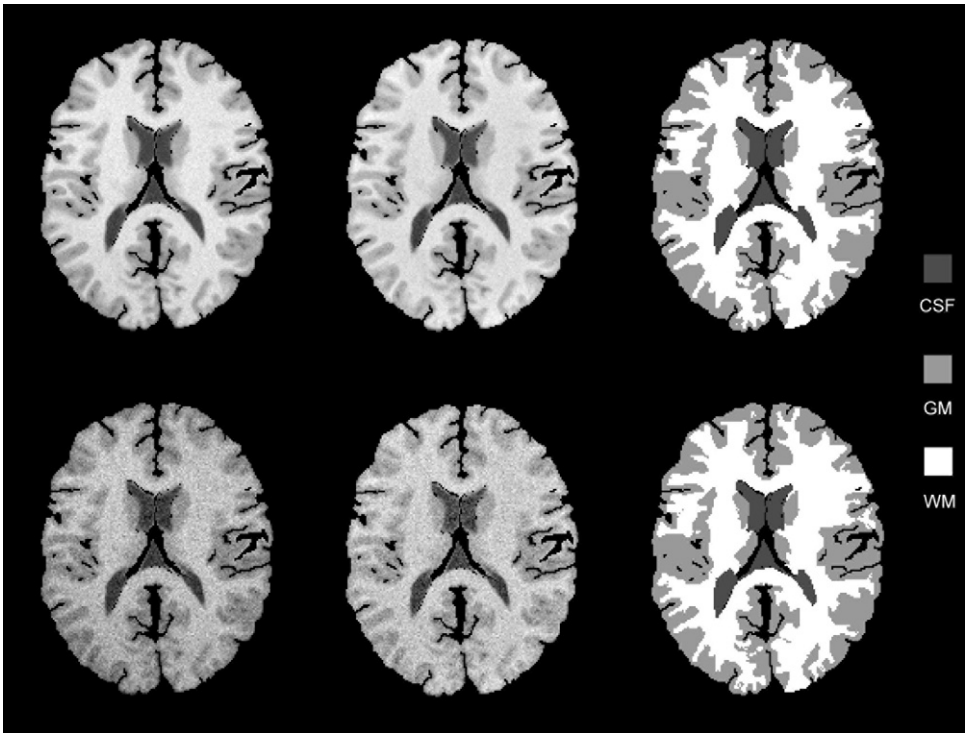

Fig. 5. The original SBMR with T1n3RF20 and T1n9RF40 images, corrected with MSR and segmented with BDT.

Table 2
Accuracy rates (ARs) and similar indices (SIs) of segmentation using the BDT algorithm with spatial feature (G, x, y, r, θ) from SBMR images with T1n3RF20, T1n5RF20, T1n7RF20, and T1n9Rf20.

		GM			WM			CSF		
		Non MSR	With MSR	EM	Non MSR	With MSR	EM	Non MSR	With MSR	EM
T1n3RF20	AR	0.9839	0.9849	0.9329	0.9771	0.9883	0.8314	0.9907	0.9962	0.7972
	SI	0.9797	0.9866	0.8654	0.9811	0.9875	0.8921	0.9879	0.9907	0.7863
T1n5RF20	AR	0.9822	0.9847	0.8986	0.9687	0.9870	0.8535	0.9888	0.9953	0.8000
	SI	0.9742	0.9858	0.8585	0.9759	0.9867	0.8929	0.9852	0.9898	0.7721
T1n7RF20	AR	0.9775	0.9822	0.8178	0.9594	0.9826	0.8503	0.9879	0.9953	0.8222
	SI	0.9667	0.9820	0.8137	0.9691	0.9834	0.8761	0.9834	0.9894	0.6815
T1n9RF20	AR	0.9746	0.9824	0.8182	0.9443	0.9791	0.6364	0.9787	0.9953	0.8463
	SI	0.9572	0.9805	0.7252	0.9594	0.9817	0.7570	0.9759	0.9871	0.5995

Fig. 5). Spatial features (G, x, y, r, θ) and (S, x, y, r, θ) were successfully applied as inputs of the BDT algorithm for SBMR images, improving the accuracy of segmentation.

Across SBMR images with different noise levels and RF inhomogeneities, the segmentation accuracy rates of the BDT algorithm with spatial features (G, x, y, r, θ) and (S, x, y, r, θ) were higher than those of the CART algorithm with spatial features (G, x, y, r, θ) and (S, x, y, r, θ). Segmentation accuracy rates of the MSRBDT by spatial features (G, x, y, r, θ) and (S, x, y, r, θ) were significantly higher than those of the CART combined with the MSR algorithm. When noise levels of brain MR images were increased, segmentation accuracy rates of the BDT algorithm with spatial features (G, x, y, r, θ) and (S, x, y, r, θ) decreased. A decrease in accuracy rates was also found when the noise levels were increased with 20% or 40% RF inhomogeneities. Applying the BDT combined with MSR algorithm, the segmentation accuracy rates did not show significant differences between SBMR images with 20% and 40% inhomogeneities. For SBMR images with noise and 20%/40% RF inhomogeneities,

Table 3
ARs and SIs of segmentation using the BDT algorithm with spatial feature (G, x, y, r, θ) from SBMR images with T1n3RF40, T1n5RF40, T1n7RF40, and T1n9Rf40.

		GM			WM			CSF		
		Non MSR	With MSR	EM	Non MSR	With MSR	EM	Non MSR	With MSR	EM
T1n3RF40	AR	0.9853	0.9844	0.9514	0.9743	0.9880	0.7438	0.9888	0.9962	0.7630
	SI	0.9787	0.9861	0.8332	0.9801	0.9871	0.8404	0.9879	0.9917	0.8000
T1n5RF40	AR	0.9812	0.9841	0.8786	0.9671	0.9867	0.8374	0.9851	0.9953	0.8056
	SI	0.9726	0.9852	0.8405	0.9745	0.9863	0.8801	0.9847	0.9912	0.7721
T1n7RF40	AR	0.9753	0.9845	0.8319	0.9486	0.9855	0.7433	0.9814	0.9925	0.8333
	SI	0.9597	0.9850	0.7745	0.9621	0.9857	0.8275	0.9787	0.9875	0.6329
T1n9RF40	AR	0.9721	0.9826	0.8077	0.9386	0.9795	0.6591	0.9796	0.9944	0.8333
	SI	0.9528	0.9809	0.7270	0.9554	0.9819	0.7699	0.9769	0.9857	0.5927

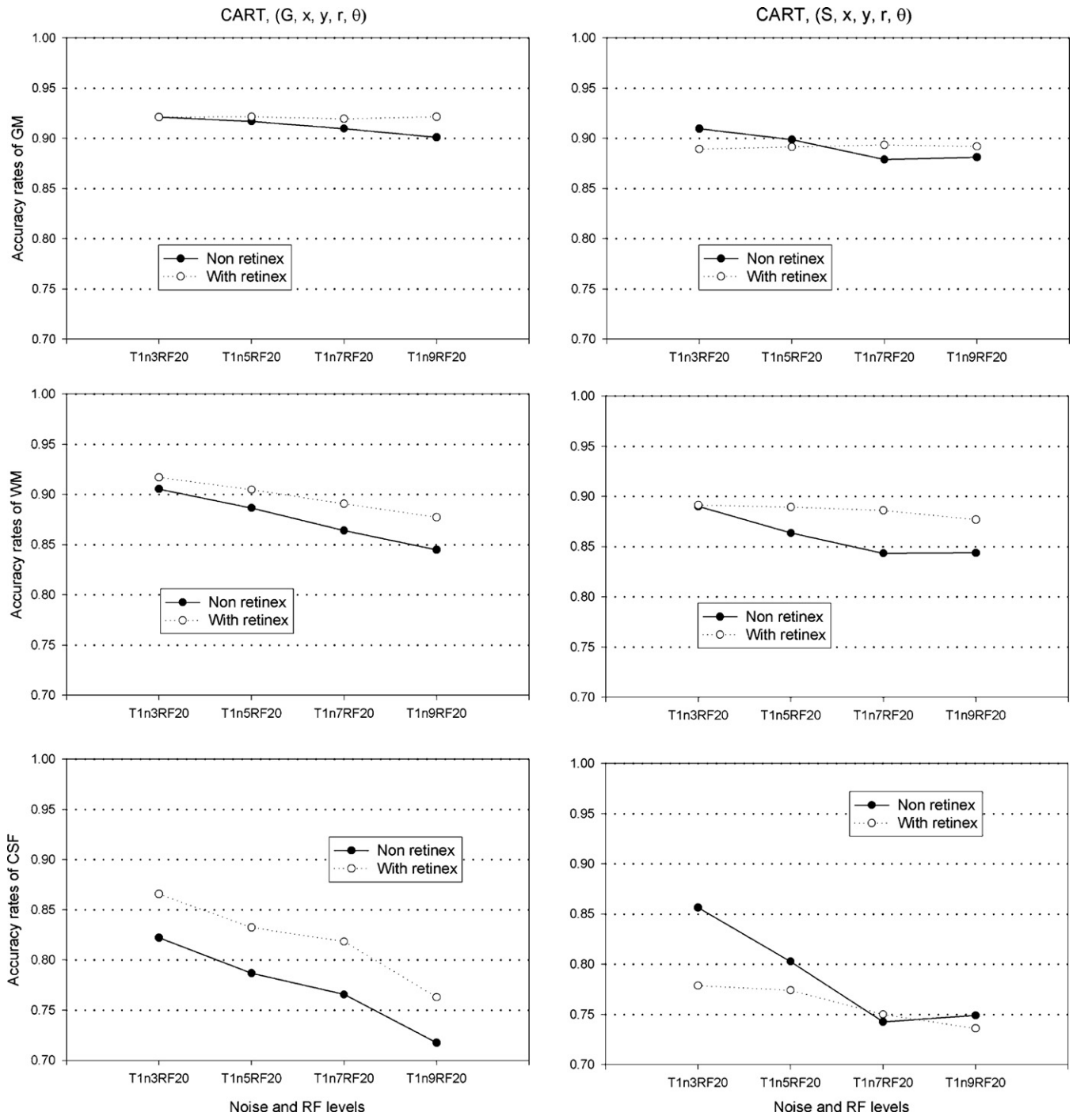

Fig. 6. Accuracy rates of tissue segmentation using CART on SBMR images with T1n3RF20, T1n5RF20, T1n7RF20, and T1n9RF20. Row 1, accuracy rates of GM. Row 2, accuracy rates of WM. Row 2, accuracy rates of CSF. Column 1, segmentation using CART with spatial feature (G, x, y, r, θ). Column 2, segmentation using CART with spatial feature (S, x, y, r, θ).

higher segmentation accuracy rates were attained by the BDT combined with MSR algorithm, with spatial features (G, x, y, r, θ) and (S, x, y, r, θ). The maximum segmentation accuracy rate was obtained with the BDT combined with MSR algorithm, with spatial feature (G, x, y, r, θ), on SBMR images with noise and 20%/40% RF inhomogeneities (see Figs. 6–9).

Accuracy rate (AR) and similar index (SI) were used to evaluate the segmentation results of SBMR images. Segmentation results were compared among the BDT only, BDT combined with the MSR algorithm, and the EM algorithm. The ARs and SIs of GM, WM, and CSF segmentation using BDT algorithm with spatial feature (G, x, y, r, θ) were higher than those in which the EM algorithm was applied. The SIs and ARs of GM, WM, and CSF segmentation using BDT combined with MSR algorithm, with spatial feature (G, x, y, r, θ), were significantly higher than those obtained with the EM algorithm (see Tables 2 and 3). For SBMR images with noise and 20%/40% RF inhomogeneities, ARs and SIs of GM, WM, and CSF segmentation using BDT combined with MSR algorithm, with spatial feature (G, x, y, r, θ), were higher than 0.9791 and 0.9805, respectively (see Tables 2 and 3). In light of the importance of brain tissue segmentation in MR images, studies have explored measures to improve the accuracy rates of MR segmentation [9,10]. Shen et al. [9] used an

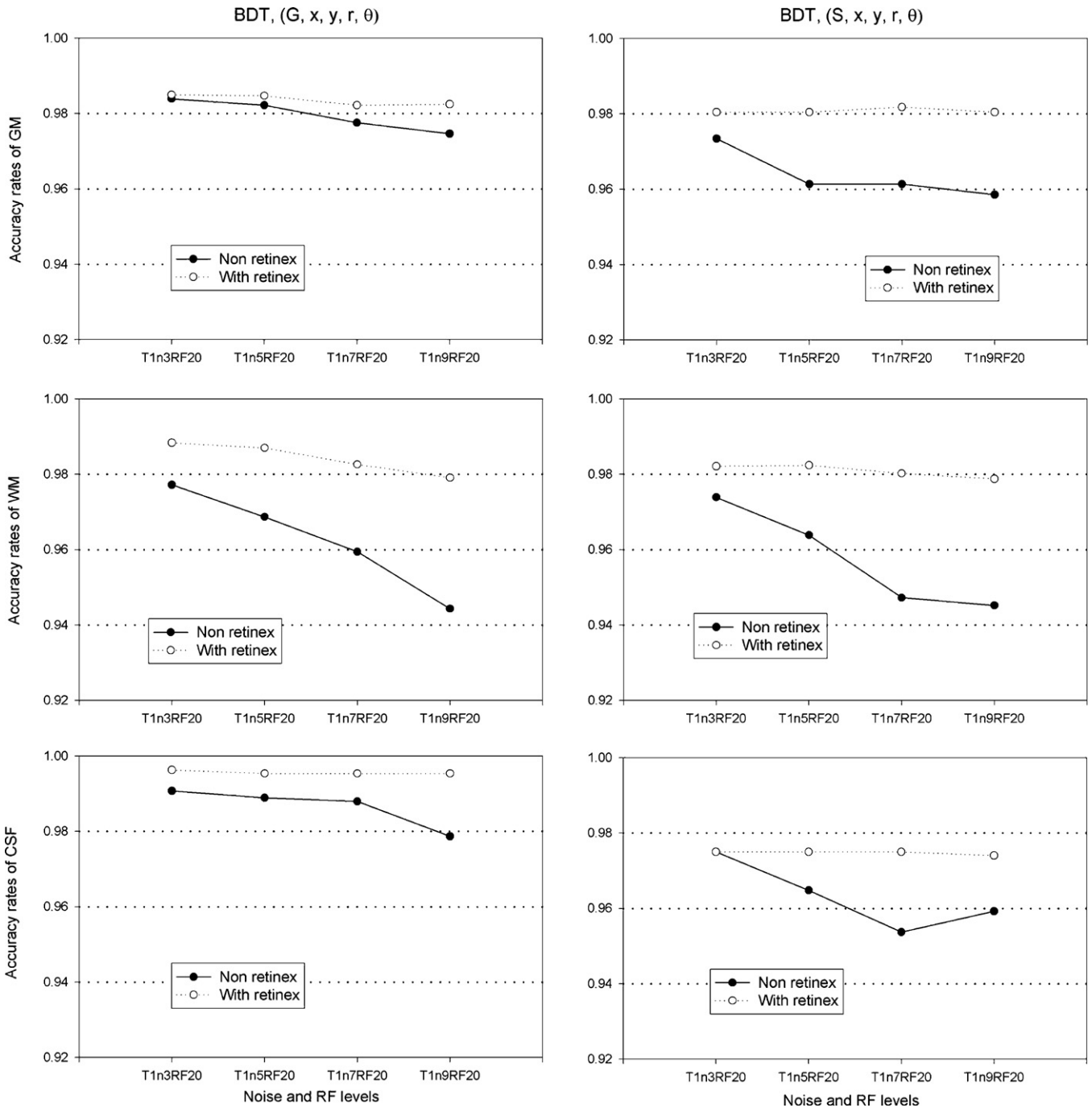

Fig. 7. Accuracy rates of tissue segmentation using a BDT algorithm on SBMR images with T1n3RF20, T1n5RF20, T1n7RF20, and T1n9RF20. Row 1, accuracy rates of GM. Row 2, accuracy rates of WM. Row 2, accuracy rates of CSF. Column 1, segmentation using BDT with spatial feature (G, x, y, r, θ). Column 2, segmentation using BDT with spatial feature (S, x, y, r, θ).

intelligent segmentation technique (IFCM) to classify GM, WM, and CSF of brain MR images according to scores, 0.85 (GM), 0.92 (WM), and 0.88 (CSF). Vrooman et al. [10] proposed a fully automatic KNN to segment brain tissues; the similar indices were 0.92 (GM), 0.92 (WM), and 0.93 (CSF). Li et al. [35] used the partial volume with combining a robust maximum a prior (PV-MAP) probability, the fuzzy C-mean (FCM), and the adaptive fuzzy C-mean (AFCM) to segment T1 weighted and T2 weighted brain MR images. The true positive fraction (TPF) of WM, GM, and CSF segmentation using AFCM was 76.58, 85.80, and 93.26, respectively. Vrooman et al. [10] used N3 algorithm to correct the RF inhomogeneity of brain MR images and then the simulated brain MR images were segmented with KNN method. The SIs were 0.93, 0.92, and 0.92 for CSF, GM, WM, respectively. These studies showed the importance of improving brain tissue segmentation accuracy in MR images. Scores of brain tissue (GM, WM, and CSF) segmentation with the present algorithm, with spatial features (G, x, y, r, θ) and (S, x, y, r, θ), were better than those in previous studies.

Other complicated MRI data sets from the Internet Brain Segmentation Repository (IBSR; http://www.cma.mgh.harvard.edu/ibsr/) were also adopted. The data consisted of 20 normal T1-weighted brains in an 8-bit format. Three selected T1-weighted brain slices (slice number 100_23, 12_3, 13_3) were segmented utilizing the MSRBDT and

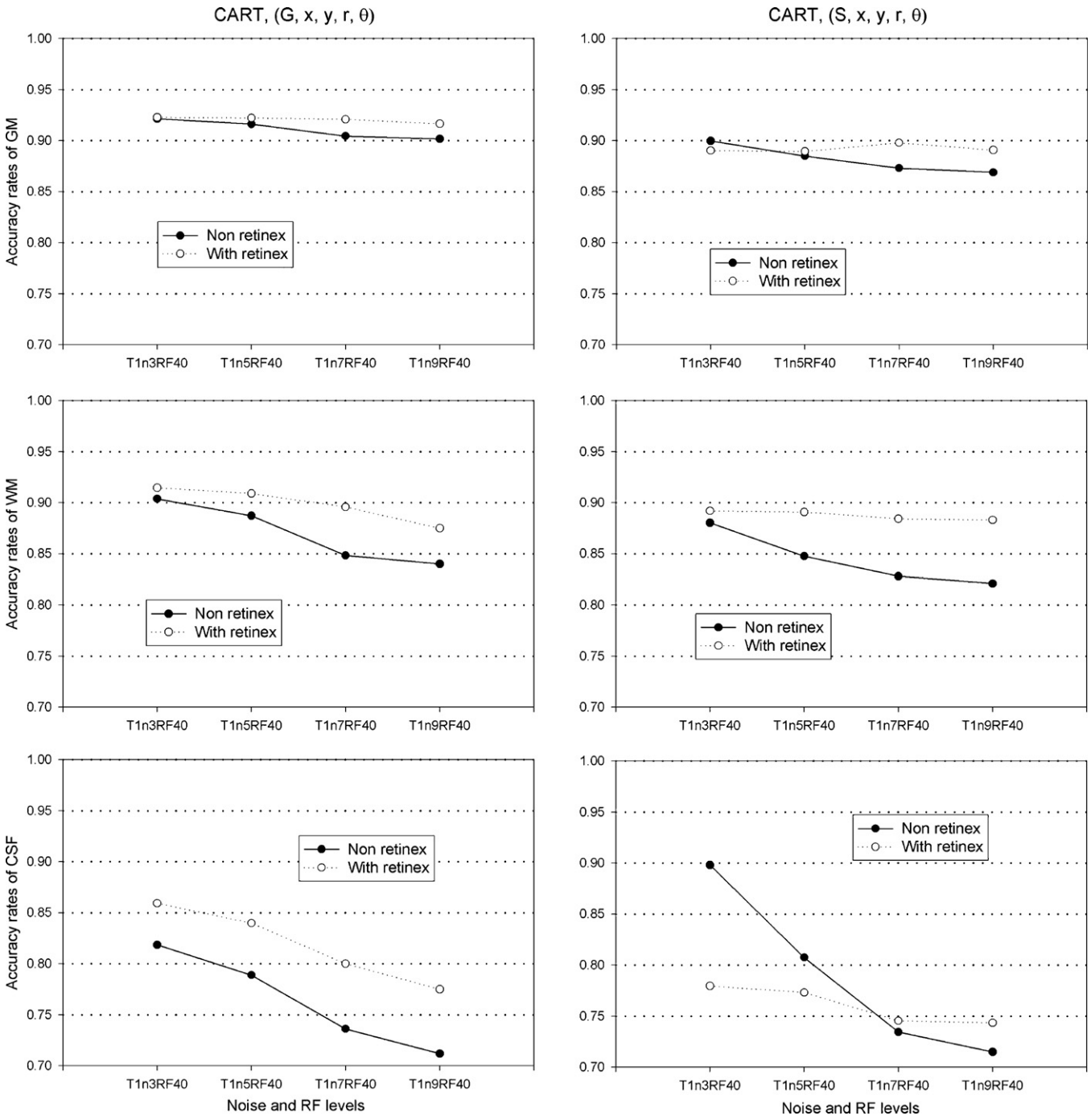

Fig. 8. Accuracy rates of tissue segmentation using CART on SBMR images with T1n3RF40, T1n5RF40, T1n7RF40, and T1n9RF40. Row 1, accuracy rates of GM. Row 2, accuracy rates of WM. Row 3, accuracy rates of CSF. Column 1, segmentation using CART with spatial feature (G, x, y, r, θ). Column 2, segmentation using CART with spatial feature (S, x, y, r, θ).

EM algorithms. The ARs and SIs of MRI segmentation when using MSRBDT with spatial features (G, x, y, r, θ) were more improved (5–15% and 6–26%, respectively) than those of segmentation when using EM with spatial features (G, x, y, r, θ). Yu et al. [36] used the same IBSR data sets to demonstrate brain image segmentation with a hybrid model-based method. A comparison of the performance of brain segmentation between MSRBDT with spatial features (G, x, y, r, θ) and the hybrid model-based method was also performed, with our proposed method attaining higher SIs of segmentation and achieving 1.3–3.8% in improvements for WM and GM segmentations – results surpassing those of segmentation by [36]. As such, better results were obtained with the MSRBDT algorithm.

In conclusion, the MSRBDT algorithm successfully segmented the SBMR images, and significantly improved the ARs and SIs of brain tissue segmentation. A supervised approach for segmentation created clearer brain tissue MR images, in which structures of interest were precisely identified by the BDT combined with MSR algorithm. In order to compare MR image segmentation accuracy rates, spatial features (G, x, y, r, θ) and (S, x, y, r, θ) were applied

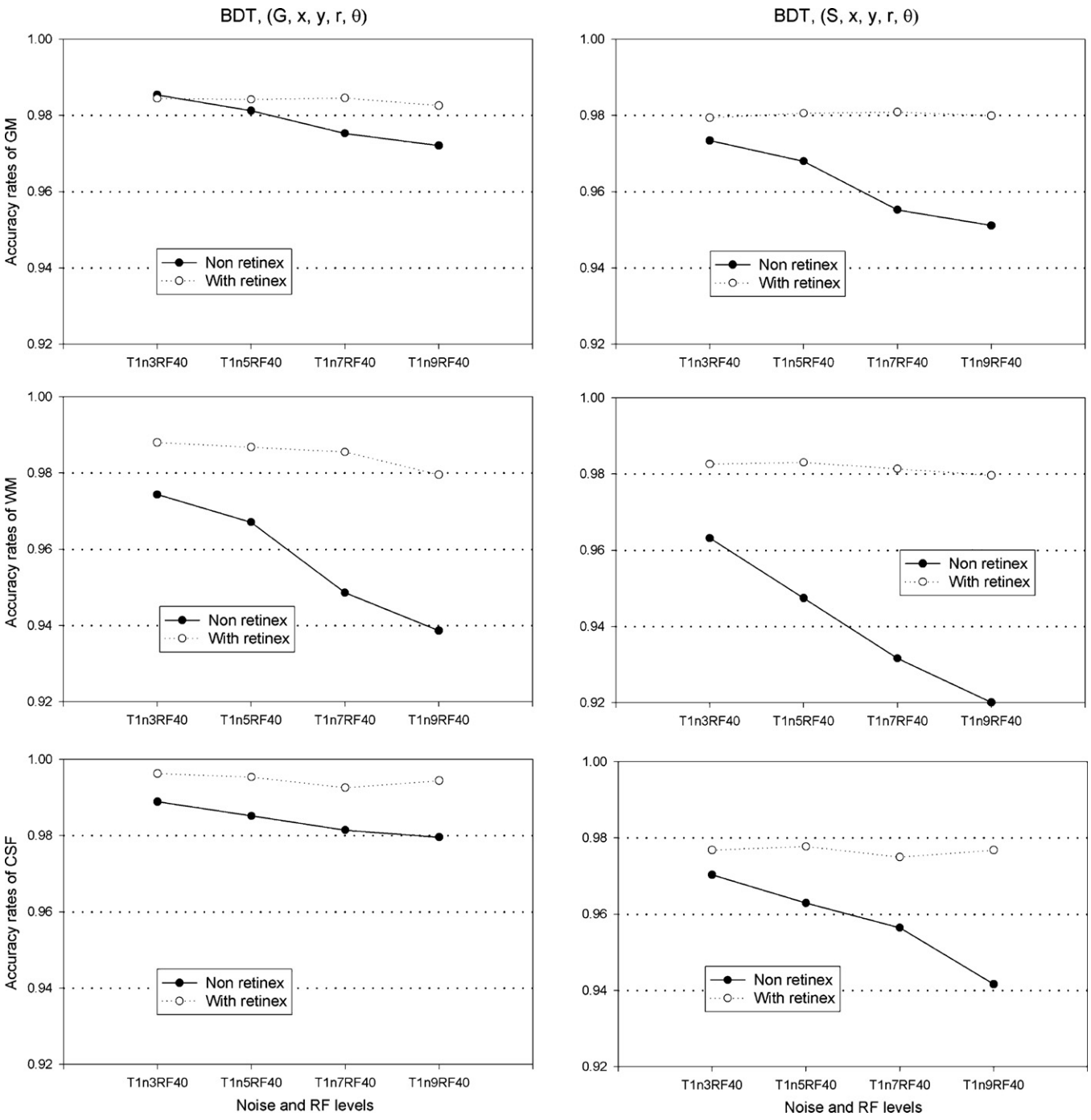

Fig. 9. Accuracy rates of tissue segmentation using a BDT algorithm on SBMR images with T1n3RF40, T1n5RF40, T1n7RF40, and T1n9RF40. Row 1, accuracy rates of GM. Row 2, accuracy rates of WM. Row 3, accuracy rates of CSF. Column 1, segmentation using BDT with spatial feature (G, x, y, r, θ). Column 2, segmentation using BDT with spatial feature (S, x, y, r, θ).

among the general gray level and spatial gray level, combined with Euclidean coordinates (x, y) or polar coordinates (r, θ) for image preprocessing. Results of segmentation evaluation indicated that the RF inhomogeneities of MR images were successfully corrected with the MSR algorithm. The optimum accuracy rates of brain tissue segmentation were obtained when the spatial feature (G, x, y, r, θ) was used to classify the SBMR images. Accuracy on SBMR images was improved when the BDT combined with MSR algorithm was applied. Therefore, the proposed BDT combined with MSR algorithm was feasible for tissue (GM, WM, and CSF) segmentation of brain MR images.

Acknowledgments

This study was supported by grant NSC 99-2628-E-010-002 and NSC 99-2221-E-264-006 from the National Science Council of the Republic of China and grant VGHUST99-P4-16 from VGHUST Joint Research Program, Tsou's Foundation.

References

[1] D. Dong-yong, B. Condon, D. Hadley, R. Rampling, G. Teasdale, Intracranial deformation caused by brain tumors: assessment of 3-D surface by magnetic resonance imaging, IEEE Trans. Med. Imaging 12 (1993) 693–702.

[2] M.R. Kaus, S.K. Warfield, A. Nabavi, P.M. Black, F.A. Jolesz, R. Kikinis, Automated segmentation of MR images of brain tumors, Radiology 218 (2001) 586–591.
[3] M. Prastawa, E. Bullitt, S. Ho, G. Gerig, A brain tumor segmentation framework based on outlier detection, Med. Image Anal. 8 (2004) 275–283.
[4] W.B. Dou, S. Ruan, Y.P. Chen, D. Bloyet, J.M. Constans, A framework of fuzzy information fusion for the segmentation of brain tumor tissues on MR images, Image Vis. Comput. 25 (2007) 164–171.
[5] L. Zhengrong, J.R. MacFall, D.P. Harrington, Parameter estimation and tissue segmentation from multispectral MR images, IEEE Trans. Med. Imaging 13 (1994) 441–449.
[6] C. Baillard, P. Hellier, C. Barillot, Segmentation of brain 3D MR images using level sets and dense registration, Med. Image Anal. 5 (2001) 185–194.
[7] C. Lukas, H.K. Hahn, B. Bellenberg, J. Rexilius, G. Schmid, S.K. Schimrigk, et al., Sensitivity and reproducibility of a new fast 3D segmentation technique for clinical MR-based brain volumetry in multiple sclerosis, Neuroradiology 46 (2004) 906–915.
[8] T. Song, C. Gasparovic, N. Andreasen, J. Bockholt, M. Jamshidi, R.R. Lee, et al., A hybrid tissue segmentation approach for brain MR images, Med. Biol. Eng. Comput. 44 (2006) 242–249.
[9] S. Shen, W. Sandham, M. Granat, A. Sterr, MRI fuzzy segmentation of brain tissue using neighborhood attraction with neural-network optimization, IEEE Trans. Inf. Technol. Biomed. 9 (2005) 459–467.
[10] H.A. Vrooman, C.A. Cocosco, F. van der Lijn, R. Stokking, M.A. Ikram, M.W. Vernooij, et al., Multi-spectral brain tissue segmentation using automatically trained k-Nearest-Neighbor classification, Neuroimage 37 (2007) 71–81.
[11] J.V. Manjon, J. Tohka, G. Garcia-Marti, J. Carbonell-Caballero, J.J. Lull, L. Marti-Bonmati, et al., Robust MRI brain tissue parameter estimation by multistage outlier rejection, Magn. Reson. Med. 59 (2008) 866–873.
[12] L.Q. Zhou, Y.M. Zhu, C. Bergot, A.M. Laval-Leantet, V. Bousson, J.D. Laredo, et al., A method of radio-frequency inhomogeneity correction for brain tissue segmentation in MRI, Comput. Med. Imaging Graph. 25 (2001) 379–389.
[13] J.D. Gispert, S. Reig, J. Pascau, J.J. Vaquero, P. García-Barreno, M. Desco, Method for bias field correction of brain T1-weighted magnetic resonance images minimizing segmentation error, Hum. Brain Mapp. 22 (2004) 133–144.
[14] M. Garcia-Sebastian, C. Hernandez, A. d'Anjou, Robustness of an adaptive MRI segmentation algorithm parametric intensity inhomogeneity modeling, Neurocomputing 72 (2009) 2146–2152.
[15] W.H. Chao, Y.Y. Chen, C.W. Cho, S.H. Lin, Y.Y. Shih, S. Tsang, Improving segmentation accuracy for magnetic resonance imaging using a boosted decision tree, J. Neurosci. Methods 175 (2008) 206–217.
[16] E. Land, An alternative technique for the computation of the designator in the retinex theory of color vision, Proc. Natl. Acad. Sci. U. S. A. 83 (1986) 3078–3080.
[17] A.C. Hurlbert, T. Poggio, Synthesizing a color algorithm from examples, Science 239 (1988) 482–485.
[18] A.C. Hurlbert, The computation of color, Ph.D. dissertation, Massachusetts Institute of Technology, Cambridge, MA, 1989.
[19] A. Moore, J. Allman, R.M. Goodman, A real-time neural system for color constancy, IEEE Trans. Neural Netw. 2 (1991) 237–247.
[20] A. Moore, G. Fox, J. Allman, R.M. Goodman, A VLSI neural network for color constancy, in: D.S. Touretzky, R. Lippman, E.S. Mateo (Eds.), Advances in Neural Information Processing 3, Morgan Kaufmann, CA, 1991, pp. 370–376.
[21] D.J. Jobson, Z. Rahman, G.A. Woodell, Properties and performance of a center/surround retinex, IEEE Trans. Image Process. 6 (1997) 451–462.
[22] D.J. Jobson, Z. Rahman, G.A. Woodell, A multiscale retinex for bridging the gap between color images and the human observation of scenes, IEEE Trans. Image Process. 6 (1997) 965–976.
[23] K.A. Grajski, L. Breiman, G. Viana Di Prisco, W.J. Freeman, Classification of EEG spatial patterns with a tree-structured methodology: CART, IEEE Trans. Biomed. Eng. 33 (1986) 1076–1086.
[24] H.R. Bittencourt, R.T. Clarke, Use of classification and regression trees (CART) to classify remotely-sensed digital images, in: Proceedings of the IEEE International Geoscience and Remote Sensing Symposium, vol. 6, 2003, pp. 3751–3753.
[25] S. Hautaniemi, S. Kharait, A. Iwabu, A. Wells, D.A. Lauffenburger, Modeling of signal-response cascades using decision tree analysis, Bioinformatics 21 (2005) 2027–2035.
[26] W.H. Chao, Y.Y. Chen, S.H. Lin, Y.Y.I. Shih, S. Tsang, Automatic segmentation of magnetic resonance images using a decision tree with spatial information, Comput. Med. Imaging Graph. 33 (2009) 111–121.
[27] J.R. Quinlan, C4. 5: Programs for Machine Learning, Morgan Kaufmann, San Mateo, CA, 1993.
[28] J.R. Quinlan, Improved use of continuous attributes in C4.5, J. Artif. Intell. Res. 4 (1996) 77–90.
[29] J.R. Quinlan, Data Mining Tools See5 and C5. 0, RuleQuest Research, Austria, 2003, http://www.rulequest.com/see5-info.html.
[30] J.R. Quinlan, Induction of decision tree, Mach. Learn. 1 (1986) 81–106.
[31] J. Macek, Incremental learning of ensemble classifiers on ECG data, in: Proceedings of the 18th IEEE Symposium on Computer-Based Medical System (CBMS'05), 2005.
[32] D. Arditi, T. Pulket, Predicting the outcome of construction litigation using boosted decision trees, J. Comput. Civil Eng. 19 (2005) 387–393.
[33] U. Amato, M. Larobina, A. Antoniadis, B. Alfano, Segmentation of magnetic resonance brain images through discriminant analysis, J. Neurosci. Methods 131 (2003) 65–74.
[34] W.M. Wells, W.E.L. Grimson, R. Kikinis, F.A. Jolesz, Adaptive segmentation of MRI data, IEEE Trans. Med. Imaging 15 (1996) 429–442.
[35] X. Li, L. Li, H. Lu, Z. Liang, Partial volume segmentation of brain magnetic resonance images based on maximum a posteriori probability, Med. Phys. 32 (2005) 2337–2345.
[36] Z.Q. Yu, Y. Zhu, J. Yang, Y.M. Zhu, A hybrid region-boundary model for cerebral cortical segmentation in MRI, Comput. Med. Imaging Graph. 30 (2006) 197–208.
[37] R.G. Boyes, J.L. Gunter, C. Frost, A.L. Janke, T. Yeatman, D.L.G. Hill, et al., Intensity non-uniformity correction using N3 on 3-T scanners with multichannel phased array coils, NeuroImage 39 (2008) 1752–1762.